Charge density distribution of $KMnF_3$ under high pressure

S. Aoyagi,[1] S. Toda,[1] E. Nishibori,[1] Y. Kuroiwa,[2,3] Y. Ohishi,[4] M. Takata,[3,4,5] and M. Sakata[4]
[1]*Department of Applied Physics, Nagoya University, Nagoya 464-8603, Japan*
[2]*Department of Physical Science, Hiroshima University, Higashi-Hiroshima, Hiroshima 739-8526, Japan*
[3]*CREST, Japan Science and Technology Agency, Kawaguchi, Saitama 332-0012, Japan*
[4]*SPring-8/JASRI, Kouto, Sayo, Hyogo 679-5198, Japan*
[5]*RIKEN SPring-8 Center, Kouto, Sayo, Hyogo 679-5198, Japan*
(Received 2 September 2008; revised manuscript received 4 November 2008; published 8 December 2008)

The charge density distributions of $KMnF_3$ under high pressure (0.3, 1.0, 1.7, 2.7, 3.4, 4.0, 4.8, 5.7, and 6.3 GPa) were determined from the synchrotron-radiation powder-diffraction data by the maximum entropy method (MEM). The difference-MEM charge density, which represents deformations from the spherical atomic charge density for each atom, is changed by applying pressure. The excess electrons on the Mn-F bond suggesting a Mn 3*d*-F 2*p* orbital hybridization were found in the difference-MEM charge densities at 0.3 GPa. The excess electrons are localized near Mn nuclei by increasing pressure. Two types of Mn-F bonds were found in the high-pressure tetragonal phase. One is parallel and another is perpendicular to the rotation axis of the F_6 octahedra (i.e., *c* axis). The number of electrons for K, F, and Mn atoms was estimated from the MEM charge densities. The valence statuses of K atom were $+1.02e$ at 0.3 GPa and $+0.20e$ at 6.3 GPa. The valence statuses of F atom were $-0.96e$ at 0.3GPa and -0.60 and $-0.77e$ at 6.3 GPa. On the other hand, the valence status of Mn atom was virtually unchanged with pressure. This fact suggests that the electron charge transfer from F to K atom occurs with increasing pressure.

DOI: 10.1103/PhysRevB.78.224102 PACS number(s): 62.50.−p, 61.05.cp, 61.50.Ks, 07.35.+k

I. INTRODUCTION

Potassium manganese trifluoride $KMnF_3$ is an antiferromagnetic (AFM) insulator belonging to KMF_3 3*d* transition-metal perovskites (*M*=Mn, Fe, Co, and Ni) and a good example for investigation of the relationship between magnetic, electronic, and structural properties. All the KMF_3 compounds are AFM insulators and their Néel temperatures are T_N=88, 113, 114, and 275 K for *M*=Mn, Fe, Co, and Ni, respectively.[1] Their crystal structure at room temperature is the ideal cubic perovskite ($Pm\bar{3}m$).[2,3] $KMnF_3$ exhibits successive structural phase transitions from the cubic phase to the tetragonal phase ($I4/mcm$) at T_{c1}=186 K and the monoclinic phase ($P2_1/m$) at T_{c2}=91 K by rotation of the F_6 octahedra.[4,5] A subsequent ferromagnetic and structural phase transition at T_{c3}=82 K has also been reported.[1,6–8]

The lattice constant is an important parameter in determining the magnetic and the electronic properties of the KMF_3 system. The magnetic coupling constant *J* strongly depends on the *M*-*M* distance (i.e., the lattice constant), and the AFM state is stabilized by the decrease in the *M*-*M* distance.[9–11] Dovesi *et al.*[11] reported that relationship between *J* and Mn-Mn distance *R* of $KMnF_3$ is expressed as $J \sim R^{-13.9}$ under isotropic compression. The *M*-*M* distance of the cubic KMF_3 is decreased by the increase in the atomic number of the transition metal *M*.[2,3] A charge density study of the cubic KMF_3 was performed by Maslen and Spadaccini[12] from the x-ray diffraction data. They reported that the excess electrons in the 3*d* e_g (t_{2g}) orbital of *M* decrease (increase) with the shortening of the lattice constant. They also reported that the constituent atoms become electrically neutral with the shortening of the lattice constant due to the replacement of *M*.

Application of pressure, which is the most effective way to control the lattice constant, should cause the remarkable changes in the magnetic and the electronic properties of the KMF_3 system without the replacement of *M*. Actually, shifts of the magnetic and the structural phase-transition temperature with increasing pressure have been revealed by the thermal-expansion,[13] elastic wave velocity,[14] and dielectric constant measurements.[15] Pressure dependence of T_N has been reported as dT_N/dP=20 K/GPa in $KNiF_3$.[13] In $KMnF_3$, pressure dependence of T_{c1} has been reported as $dT_{c1}/dP \approx 30$ K/GPa,[14,15] and the pressure-induced structural phase transition from the cubic to the tetragonal phase has been observed at around 3.1 GPa at room temperature.[16,17]

Electron charge density distributions under high pressure will provide essential information on the relationship between the crystal structure and the electronic/magnetic properties of the KMF_3 system. We have investigated the charge density distributions of the other cubic perovskites, such as $BaTiO_3$, $PbTiO_3$, etc.,[18–20] using the synchrotron-radiation (SR) powder-diffraction[21] and the maximum entropy method (MEM).[22] The characteristic features which can be connected with the ferroelectric/antiferroelectric properties have been observed in the MEM charge densities.[18–20] Pressure effects on the electronic structure such as the chemical bonding nature, the 3*d* orbital state of *M*, and the atomic charges in the KMF_3 system are extremely interesting with conjunction of these previous studies.

The aim of the present study is to investigate the pressure effects on the electronic structure of $KMnF_3$ by an accurate charge density distribution. For that purpose, the SR powder diffraction under high pressure using a diamond-anvil cell (DAC) and the MEM (Ref. 22) charge density analysis were adopted. It is normally difficult to obtain adequate diffraction data for the charge density study using a DAC because a sample loaded into the DAC is only a few micrograms and the maximum diffraction angle is limited by the cell aperture.

TABLE I. Experimental conditions of the powder-diffraction experiment of $KMnF_3$ under high pressure using a DAC. The experiments were carried out at BL10XU, SPring-8.

Culet size	1 mm in diameter
Gasket	0.1-mm-thick stainless steel
Gasket hole	0.5 mm in diameter
Pressure medium	4:1 methanol-ethanol mixture
Pressure determination	Ruby fluorescence method
Pressure	0.3, 1.0, 1.7, 2.7, 3.4, 4.0, 4.8, 5.7, and 6.3 GPa
Temperature	Room temperature
X-ray wavelength	0.494 Å
X-ray beam size	0.2 mm in diameter
Exposure time	6 min for data A and 12 min for data B

The high-energy SR powder diffraction can overcome the above difficulties and enables us to collect accurate diffraction data with high counting statistics and high real-space resolution from a sample. The MEM is a powerful method to obtain a charge density distribution from x-ray diffraction data.[18–20,22–26] For example, the charge density studies of a gold complex $Cs_2Au_2Br_6$ and a bilayered manganite $La_{1.04}Sr_{1.96}Mn_2O_7$ under high pressure have been successfully performed by the SR powder diffraction and the MEM analysis.[25,26] In this paper, we report the results of the charge density study of $KMnF_3$ under high pressure.

II. EXPERIMENT

The high-pressure diffraction experiments were performed using a DAC at the undulator beamline BL10XU, SPring-8 (Hyogo, Japan). Powder-diffraction patterns of $KMnF_3$ were collected using a flat imaging plate (IP) detector (1 pixel=0.10 mm). The experimental conditions are summarized in Table I. We measured two diffraction patterns with different sample-detector distance (data A and B) at each pressure to estimate the distance between a sample and the IP surface (camera length). During the measurement, the DAC oscillated around the vertical axis by $\pm 4°$ to increase powder particles which contribute to scattering. The exposed IPs were read after waiting for 5 min to suppress the fading effect of IP.[27]

One-dimensional powder-diffraction patterns were obtained by integrating horizontal equatorial profiles of the two-dimensional diffraction patterns. Twelve horizontal lines around equatorial line were integrated. Diffraction angles 2θ were calculated from the horizontal positions of each pixel and the camera lengths. The camera lengths were accurately determined from several diffraction-peak positions of data A and B.

Intensity corrections for Lorentz, angular step size, polarization, absorption, and oblique incidence were applied to the one-dimensional powder-diffraction patterns. The Lorentz factor and the correction for angular step size in the flat IP geometry are given in Ref. 28. The polarization factor for the horizontally polarized incident beam was $\cos^2 2\theta$. Absorption effects for $KMnF_3$ powder sample, pressure medium, diamond anvil, and air were taken into account in the absorption correction. The correction for oblique incidence of the diffraction beam on the flat IP is expressed as $[1-\exp(\ln T_{IP}/\cos 2\theta)]/(1-T_{IP})$, where T_{IP} is the transmission factor of the phosphor layer of the IP at the normal incidence.[29] T_{IP} was estimated from powder-diffraction patterns of CeO_2 standard sample (NIST SRM 674a). The determined value of T_{IP} for wavelength 0.494 Å was 0.74 (3).

III. STRUCTURAL CHANGES UNDER HIGH PRESSURE

The pressure dependence of (200) profile observed in data B is shown in Fig. 1. The peak position shifts to high angle as increasing pressure by lattice contraction. Obvious peak splitting suggesting tetragonal lattice strain, as shown in profile at 5.7 GPa in Fig. 1, was observed above 4.0 GPa. The profile after pressure release from 6.3 to 0.0 GPa is also shown in Fig. 1. The peak shape and the peak position at 0.0 GPa are almost identical to the shape at 0.3 GPa. This fact indicates that the pressure effect is reversible. We confirmed pressure reversibility of the structure by Rietveld refinement of 0.0 GPa data.

An alternate rotation of the F_6 octahedra around c axis appears in the tetragonal phase, and hence a $\sqrt{2}a \times \sqrt{2}b \times 2c$ superstructure is formed. The superlattice reflections appeared at 3.4 GPa. The transition pressure P_c was estimated from the pressure dependence of the integrated intensities I of (3/2 1/2 1/2), (3/2 1/2 3/2), and (3/2 1/2 5/2) superlattice reflections using the power law $I=A(P-P_c)^{0.5}$.[17] The estimated P_c is 3.2(1) GPa, which is consistent with the previous works.[17]

The one-dimensional diffraction patterns obtained from the data A with the 2θ range of $3-40°$ ($d>0.73$ Å) were analyzed by the Rietveld method using the SP (Ref. 24) software. The cubic and the tetragonal structure models were used in the Rietveld analysis for the data below and above P_c, respectively. In the structure models, the ionic spherical scattering factors for K^+, Mn^{2+}, and F^- from Ref. 30 were adopted. The reliability factors were always better in the analysis for any data by using the ionic scattering factors than the neutral ones. The thermal displacement parameters

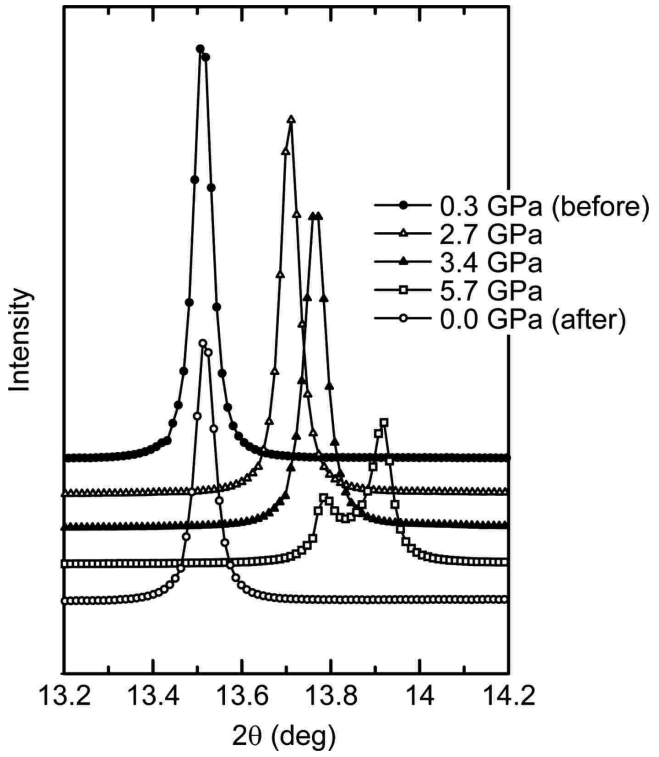

FIG. 1. Observed (200) profiles in data B at 0.3, 2.7, 3.4, and 5.7 GPa. The profile after pressure release from 6.3 to 0.0 GPa is also shown as open circle.

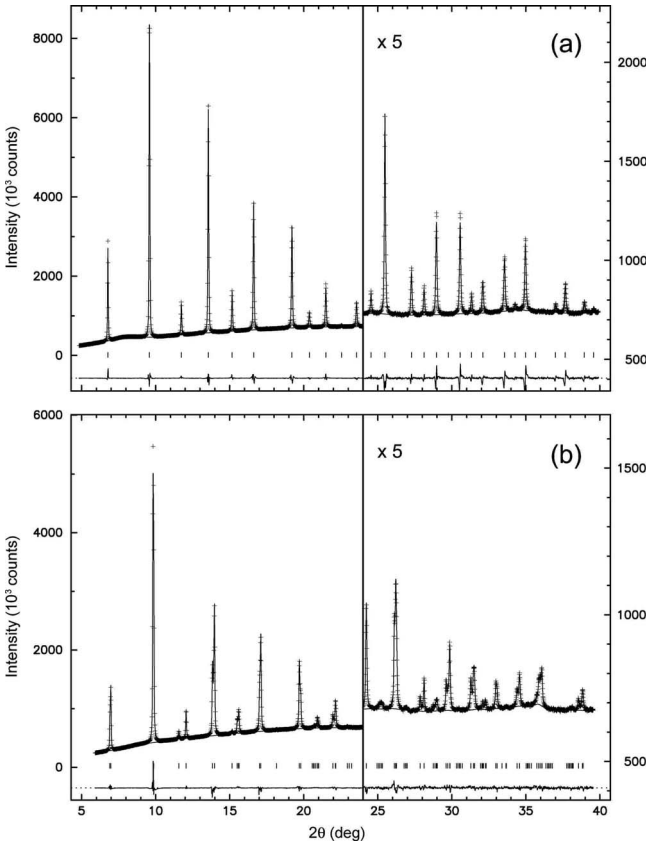

FIG. 2. Final Rietveld fitting results of $KMnF_3$ at (a) 0.3 GPa for the cubic phase and (b) 5.7 GPa for the tetragonal phase. Observed and calculated intensities are plotted as cross marks and solid lines, respectively. Lower bar marks and solid lines indicate positions of Bragg peaks and differences between observed and calculated intensities, respectively.

were refined as isotropic for K^+ and Mn^{2+} and as anisotropic for F^-.

The split-type pseudo-Voigt function was used for modeling the peak shape.[31] Profiles below 3.4 GPa were well fitted by using symmetrical peaks. In the tetragonal phase above 4.0 GPa, peak splitting and peak shift due to the tetragonal strain accompany asymmetrical deformation of peak shape. Peak shapes above 4.0 GPa were slightly altered for individual refinement by introducing asymmetries of each peak. The widths for (111) peak at around 12° in 2θ were 0.070° for 0.3 GPa and 0.076° for 6.3 GPa, respectively. It is found that effect of the nonhydrostaticity of a pressure medium is negligibly small in the present study. We investigated pressure-induced preferred orientation in the Rietveld refinement. The reliability factors based on weighted profile R_{WP} with (001) preferred orientation correction for 6.3 GPa data was 1.13% which is almost identical to R_{WP} without correction: 1.15%. This fact indicates there is no pressure-induced preferred orientation in the present high-pressure data.

The final Rietveld fitting results for 0.3 (cubic phase) and 5.7 GPa (tetragonal phase) data are shown in Figs. 2(a) and 2(b) and the determined structural parameters for the cubic and the tetragonal phases are listed in Tables II and III together with the reliable factors, respectively.

The pressure dependence of the interatomic distances and the unit-cell volume V are shown in Figs. 3(a), 3(b), and 3(d). The pressure dependence of the rotation angle of the F_6 octahedra ϕ in the tetragonal phase is well fitted by a power law $\phi = A(P - P_c)^{0.25}$ as shown in Fig. 3(c). There are two kinds of F atoms in the tetragonal phase, which are denoted as F(1) and F(2). F(1) is on the rotation axis of the F_6 octahedra and F(2) is displaced by the rotation of the F_6 octahedra. Both the Mn-F distances $d_{\text{Mn-F(1)}}$ and $d_{\text{Mn-F(2)}}$ decrease

TABLE II. The reliability factors of Rietveld analysis and the determined structural parameters for cubic $KMnF_3$ under high pressure at room temperature. The reliability factors based on weighted profile R_{WP} and Bragg intensity R_I are listed. The structure is the perovskite type ($Pm\bar{3}m$) in which K, Mn, and F occupy the corner, the body-center, and the face-center sites, respectively. The anisotropic atomic displacement parameters for F perpendicular and parallel to the Mn-F bond are denoted as U_{11}(F) and U_{33}(F), respectively.

P (GPa)	0.3	1.0	1.7	2.7
R_{WP} (%)	1.55	1.40	1.32	1.37
R_I (%)	1.68	2.47	2.27	2.47
a (Å)	4.19298(5)	4.17304(4)	4.15058(4)	4.12959(4)
V (Å^3)	73.717(3)	72.670(2)	71.503(2)	70.424(2)
U(K) (Å^2)	0.0199(3)	0.0184(3)	0.0170(3)	0.0172(3)
U(Mn) (Å^2)	0.0071(1)	0.0061(1)	0.0065(5)	0.0066(1)
U_{11}(F) (Å^2)	0.040(1)	0.036(1)	0.038(1)	0.039(1)
U_{33}(F) (Å^2)	0.0070(7)	0.0040(6)	0.0020(6)	0.0080(6)

TABLE III. The reliability factors of Rietveld analysis and the determined structural parameters for tetragonal $KMnF_3$ under high pressure at room temperature. The structure is tetragonal with the space group $I4/mcm$ in which K, Mn, F(1), and F(2) occupy (0.5, 0, 0.25), (0, 0, 0), (0, 0, 0.25), and (0.75+δ, 0.25+δ, and 0), respectively. The anisotropic atomic displacement parameters for F were refined with constraints of $U_{11}[F(1)]=U_{33}[F(2)]=U_{11}[F(2)]+U_{12}[F(2)]$ and $U_{33}[F(1)]=U_{11}[F(2)]-U_{12}[F(2)]$.

P (GPa)	3.4	4.0	4.8	5.7	6.3
R_{WP} (%)	1.21	1.26	1.08	1.21	1.15
R_I (%)	1.44	2.74	1.37	2.08	2.21
a (Å)	5.81569(8)	5.79520(7)	5.78338(6)	5.74910(7)	5.72972(8)
c (Å)	8.2321(3)	8.2305(2)	8.2343(1)	8.2092(2)	8.2046(2)
V (Å^3)	278.43(2)	276.42(1)	275.42(1)	271.33(1)	269.36(1)
δ	0.0144(9)	0.0228(7)	0.0254(6)	0.0285(6)	0.0317(7)
U(K) (Å^2)	0.0167(3)	0.0160(3)	0.0180(3)	0.0181(3)	0.0174(3)
U(Mn) (Å^2)	0.0075(1)	0.0067(1)	0.0086(1)	0.0076(3)	0.0072(3)
U_{11}[F(1)] (Å^2)	0.036(4)	0.042(4)	0.040(3)	0.038(3)	0.038(4)
U_{33}[F(1)] (Å^2)	0.012(2)	0.006(2)	0.008(2)	0.012(2)	0.011(2)
U_{11}[F(2)] (Å^2)	0.024(7)	0.024(2)	0.024(2)	0.025(2)	0.025(2)
U_{33}[F(2)] (Å^2)	0.036(7)	0.042(3)	0.040(2)	0.038(2)	0.038(2)
U_{12}[F(2)] (Å^2)	0.012(4)	0.018(2)	0.016(2)	0.013(2)	0.013(2)

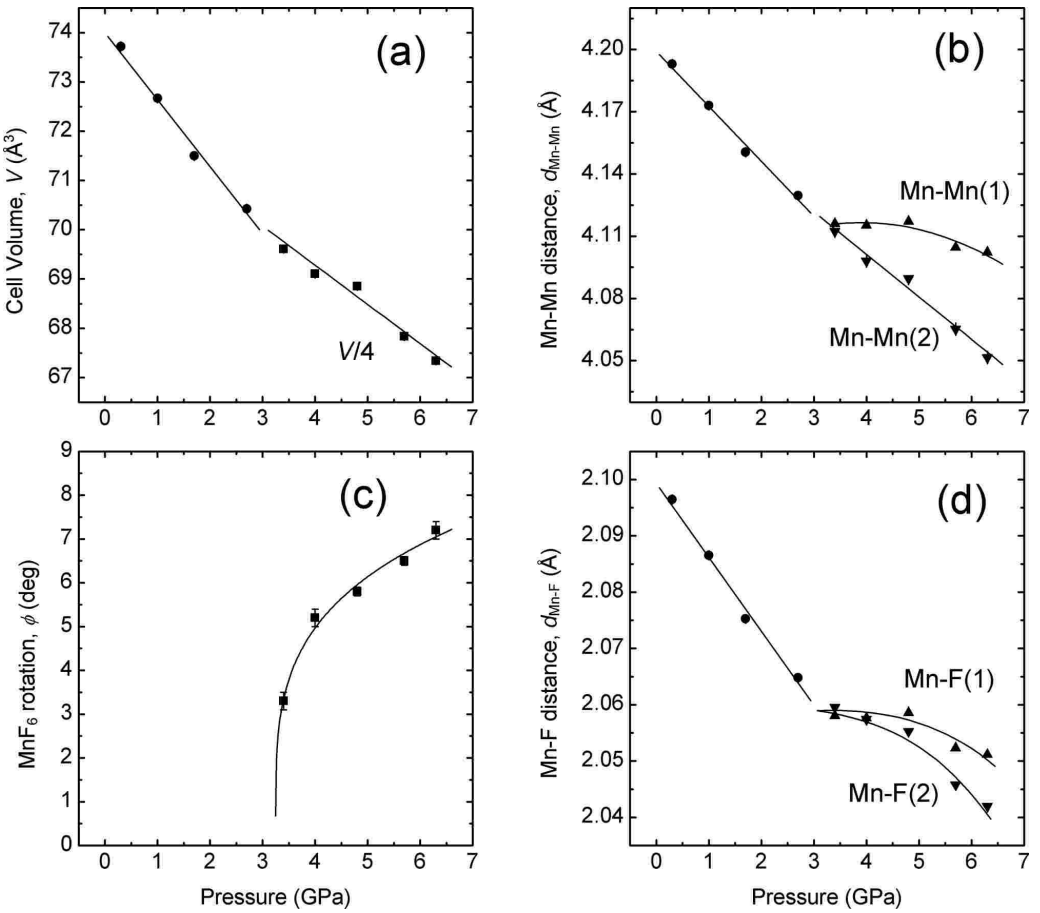

FIG. 3. Pressure dependence of (a) the unit-cell volume, (b) the Mn-Mn distance, (c) the rotation angle of the F_6 octahedra and (d) the Mn-F distance of $KMnF_3$. The unit-cell volumes of the tetragonal phase are divided by four to be comparable with the cubic phase in (a). Two kinds of Mn-Mn distances parallel and perpendicular to the rotation axis of the F_6 octahedra in the tetragonal phase are denoted as Mn-Mn(1) and Mn-Mn(2) in (b), respectively.

with pressure as shown in Fig. 3(d). $d_{\text{Mn-F(1)}}$ and $d_{\text{Mn-F(2)}}$ very gradually decrease with increasing pressure, while ϕ rapidly increases below 4.8 GPa [Figs. 3(c) and 3(d)]. This fact may be interpreted that the rotation of the F_6 octahedra prevents from the decrease in the Mn-F distances. Above 4.8 GPa, $d_{\text{Mn-F(1)}}$ and $d_{\text{Mn-F(2)}}$ rather rapidly decrease and the shape of the F_6 octahedra is distorted as $d_{\text{Mn-F(1)}}$ is longer than $d_{\text{Mn-F(2)}}$. The Mn-Mn distances parallel and perpendicular to c axis, which are denoted as $d_{\text{Mn-Mn}}(1)$ and $d_{\text{Mn-Mn}}(2)$, respectively, show different pressure dependence in the tetragonal phase [Fig. 3(b)]. The values of $d_{\text{Mn-Mn}}(1)$ are identical with $2d_{\text{Mn-F(1)}}$. Despite the complicated pressure dependence of $d_{\text{Mn-F(2)}}$, $d_{\text{Mn-Mn}}(2)$ decreases monotonically at increasing pressure. The pressure dependence of $d_{\text{Mn-Mn}}(2)$ is achieved if the rotation of the F_6 octahedra is even with the applied pressure.

IV. MEM CHARGE DENSITIES

The charge density distributions ρ_{obs} were calculated by the MEM analysis[22] using the program package ENIGMA.[32] The 24- and 77-independent observed structure factors, which were derived by the Rietveld fitting, were used in the MEM analysis for the cubic and tetragonal phases, respectively. The analysis was carried out with the unit cell divided into $84\times84\times84$ pixels in cubic case and $120\times120\times160$ pixels in tetragonal case, respectively. The MEM calculations were stopped when the reliability factor based on the structure factors R_{MEM} reached 1%.

The model charge density distributions ρ_{cal} were also calculated by the same procedure. The structure factors were calculated based on the structure models determined in the Rietveld analysis listed in Tables II and III. In the structure models, the ionic spherical scattering factors for K^+, Mn^{2+}, and F^- from Ref. 30 were adopted. The number of structure factors for ρ_{cal} was identical to that for ρ_{obs}.

An obtained MEM charge-density map in a (001) plane through Mn and F atoms at 2.7 GPa is shown in Fig. 4(a). It shows very clear charge-density overlaps between Mn and F atoms, which should be interpreted as a Mn $3d$-F $2p$ orbital hybridization.[11] The charge density at the saddle point of the Mn-F bond is $0.53e/\text{Å}^3$ at 2.7 GPa. Charge density overlap between K and F is very small. The bond distance and the charge-density at the saddle point of the K-F bond are 2.92 Å and $0.17e/\text{Å}^3$ at 2.7 GPa, respectively. The charge density distributions around F nuclei are elongated perpendicular to the Mn-F bond. This feature is consistent with the refined anisotropic thermal displacement parameters for F atom (Table II) and may be related to the rotational soft mode of the F_6 octahedra. Such an anisotropy of charge density distribution has also been found around O nuclei in cubic $PbZrO_3$ and $SrTiO_3$ which undergo the phase transition by the rotation of the oxygen octahedra.[19,20]

Figures 4(b) and 4(c) are MEM charge-density maps through Mn and F atoms at 5.7 GPa in a (001) and a (110) plane, respectively. The charge density overlap between Mn and F and the anisotropic distribution around F are found in all of the charge density distributions up to 6.3 GPa. It is clearly seen that the F_6 octahedra rotate around [001] [Fig. 4(b)]. The rotation of the F_6 octahedra causes the decrease in the K-F(2) distance. However, the charge density overlap between K and F is still small at 5.7 GPa. The bond distance and the charge-density at the saddle point of the shortest K-F bond at 5.7 GPa are 2.73 Å and $0.19e/\text{Å}^3$, respectively.

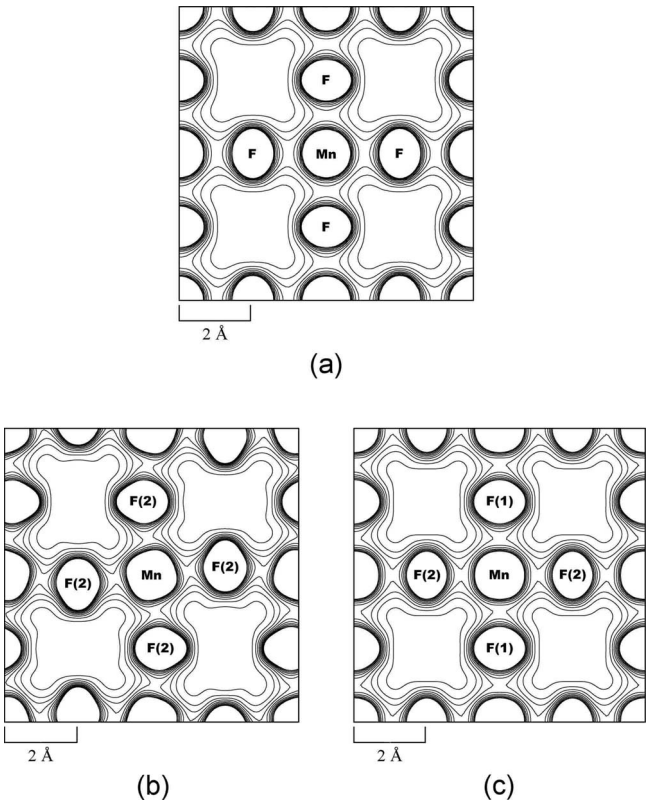

FIG. 4. MEM charge density maps of $KMnF_3$ through Mn and F for (a) the cubic phase at 2.7 GPa and (b); (c) the tetragonal phase at 5.7 GPa. The maps at 5.7 GPa on x, y, 0, and x, x, z planes are shown in (b) and (c), respectively. The contour lines are drawn from 0 to $1.5e/\text{Å}^3$ at intervals of $0.15e/\text{Å}^3$.

V. DIFFERENCE CHARGE DENSITIES

Difference-MEM charge densities $\Delta\rho=\rho_{\text{obs}}-\rho_{\text{cal}}$ were calculated to investigate the $3d$ orbital state of Mn under high pressure. The difference charge densities ($\Delta\rho$ maps) represent the various deformations from the spherical atomic charge densities.

The $\Delta\rho$ maps through Mn and F atoms at 0.3, 2.7, 3.4, and 5.7 GPa are shown in Fig. 5. Positive differences are found between Mn and F at 0.3 GPa [Fig. 5(a)], which are interpreted as bonding electrons due to the Mn $3d$-F $2p$ orbital hybridization.[11] The bonding character becomes weaker and the positive differences are localized close to Mn nuclei at 2.7 GPa [Fig. 5(b)]. The feature of the $\Delta\rho$ map is very similar to a theoretical one calculated by Dovesi *et al.*[11] Positive differences around Mn nuclei directed to F are regarded as excess electrons in $3d$ e_g orbitals.

Difference densities around Mn nuclei are changed dramatically through the pressure-induced phase transition. Doubly degenerated $3d$ e_g orbitals in the cubic phase may

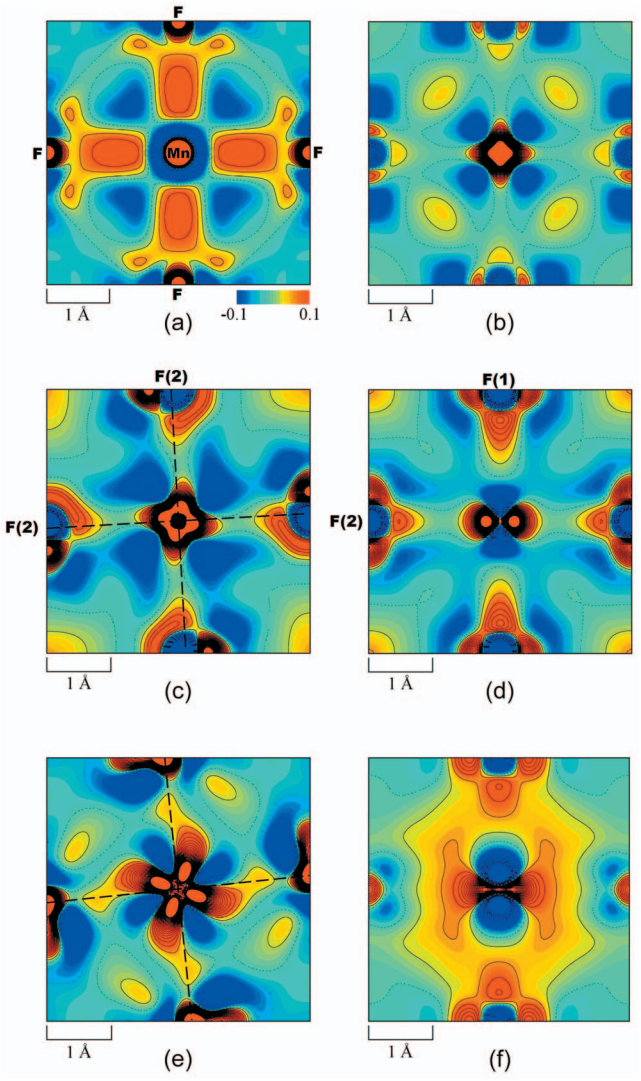

FIG. 5. (Color) Difference-MEM charge-density maps of $KMnF_3$ through Mn and F at (a) 0.3, (b) 2.7, (c), (d) 3.4 and (e), and (f) 5.7 GPa. The maps for the tetragonal phase at 3.4 (5.7) GPa on x, y, 0, and x, x, z planes are shown in (c) [(e)] and (d) [(f)], respectively. The contour lines are drawn from −0.9 to $0.9e/\text{Å}^3$ at intervals of $0.04e/\text{Å}^3$. Positive and negative differences are drawn as solid and dotted lines, respectively. Broken lines connect Mn and F(2) in (c) and (e).

split into $3dz^2$ and $3dx^2-y^2$ orbital in the tetragonal phase. As reflecting the splitting of the orbital, $\Delta\rho$ around Mn nuclei along c axis in the tetragonal phase are very different from that of perpendicular to c axis as shown in Figs. 5(c) and 5(d). Positive differences around Mn nuclei which are interpreted as excess electrons in the $3dx^2-y^2$ orbital are found in the perpendicular plane to c axis [Fig. 5(c)].

The direction of positive differences around Mn nuclei deviated from the Mn-F(2) bond direction [Fig. 5(c)]. The deviation of the extend direction of the positive differences from the Mn-F(2) bond direction becomes greater at increasing pressure [Figs. 5(c) and 5(e)]. Angles between the extend direction of the positive differences and the Mn-F(2) bond direction are about 10° and 26° at 3.4 and 5.7 GPa, respectively.

Difference densities around Mn nuclei along c axis are negative in the tetragonal phase [Figs. 5(d) and 5(f)]. The negative differences around Mn nuclei can be interpreted as depopulation of electrons in the $3dz^2$ orbital. The electrons displaced from the $3dz^2$ orbital may occupy the $3dx^2-y^2$ orbital, since the number of electrons around a Mn nucleus is preserved through the phase transition as described later.

The pressure effects on the charge densities of $KMnF_3$ found in this study are consistent with the chemical pressure effects in cubic KMF_3 (M=Mn, Fe, Co, and Ni) studied by Maslen and Spadaccini[12] by the conventional difference Fourier analysis. They reported that the height of difference densities between M and F is lowered nearly linearly with the decrease in the M-F distance due to the replacement of M. The height of difference densities between M and F is negative as $-1.1e/\text{Å}^3$ in $KNiF_3$, whereas it is positive as $0.5e/\text{Å}^3$ in $KMnF_3$.[12] The increase in antibonding character in $KNiF_3$ has been confirmed also in theoretical studies.[10,11] The decrease in excess electrons on the Mn-F bond by increasing pressure in cubic $KMnF_3$ [Figs. 5(a) and 5(b)] is similar with the above chemical pressure effect. The difference densities around Mn nuclei are changed dramatically by the pressure-induced phase transition [Figs. 5(c) and 5(d)]. The pressure dependence of the difference densities in the tetragonal phase is rather different from the chemical pressure effects and is allowed in the lower symmetry of the tetragonal phase [Figs. 5(c)–5(f)].

VI. ATOMIC CHARGES

Electron numbers around nuclei were computed from ρ_{obs} to investigate the pressure dependence of atomic charges. The region of counting electrons is the inside of planes which are perpendicular to the interatomic line and on the interatomic charge density saddle point. The atomic charges were calculated by subtracting the electron numbers from the atomic numbers. The atomic charges at 0.3 GPa are +1.02, +1.81, and $-0.96e$ for K, Mn, and F, which are close to the formal charges +1, +2, and −1. The pressure dependence of atomic charges for K, Mn, and F is summarized in Fig. 6. The atomic charges for K and F approached electrically neutral state with pressure, whereas for Mn it is almost unchanged. The atomic charges at 6.3 GPa are +0.20, +1.95, −0.60, and $-0.77e$ for K, Mn, F(1), and F(2). The pressure dependence of the atomic charges implies that the electron charge transfer from F $2p$ to K $4s$ orbital occurs with increasing pressure.

Maslen and Spadaccini[12] also reported that the atomic charges are changed linearly with the decrease in the M-F distance by the replacement of M as the constituent atoms become electrically neutral. Pressure dependence of the atomic charges of K and F in $KMnF_3$ is similar with the chemical pressure effect (see upper and lower parts of Fig. 6). The atomic charge of Mn is not changed by increasing pressure as different from the chemical pressure effect (see middle part of Fig. 6). The sum of the electronic charges of two kinds of cations in $KMnF_3$ at 6.3 GPa, which is $+2.15e$, is almost identical to that in $KNiF_3$ at ambient pressure; that is, $+2.13e$.[12] The nuclear charge of M is not changed by

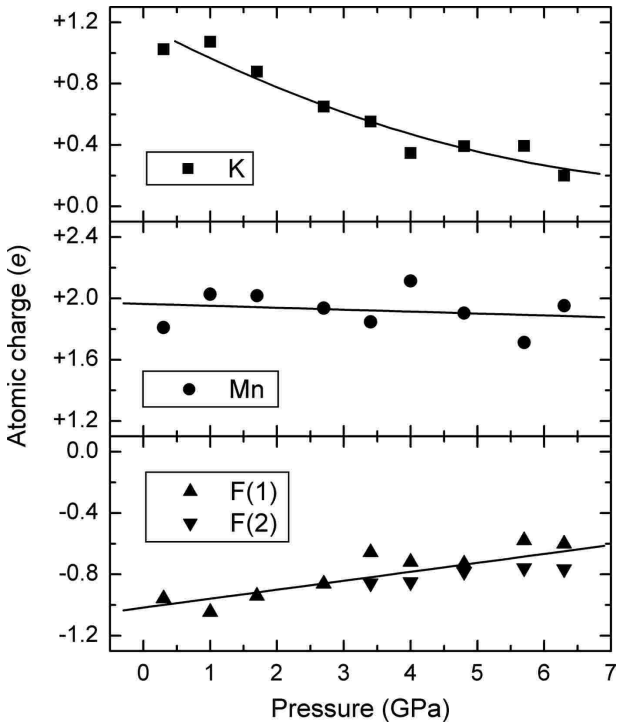

FIG. 6. Pressure dependence of the atomic charges of $KMnF_3$. The atomic charges were calculated by subtracting the electron numbers around nuclei from the atomic numbers. The atomic charges for K, Mn, and F are plotted in upper, middle, and lower panels, respectively.

increasing pressure, whereas it is changed by the replacement of M. This is a distinct difference of the chemical pressure effects and the pressure effects on the atomic charge of M.

VII. CONCLUSION

We successfully obtained MEM charge-density distributions of $KMnF_3$ under high pressure from SR powder-diffraction data with $d > 0.73$ Å. Significant pressure effects on the difference-MEM charge densities around Mn nuclei and the atomic charges of K and F were observed. Excess electrons on the Mn-F bond in the cubic phase, which are interpreted as bonding electrons due to the Mn $3d$-F $2p$ orbital hybridization, localize near Mn nuclei with increasing pressure. After the pressure-induced cubic-tetragonal phase transition, the difference densities around Mn nuclei along c axis become negative, which implies depopulation of electrons in the Mn $3dz^2$ orbital. The difference densities around Mn nuclei perpendicular to c axis are positive, which can be regarded as excess electrons in the $3dx^2-y^2$ orbital. The direction of the positive differences around Mn nuclei is deviated from the Mn-F(2) bond direction at increasing pressure. The dramatic changes of the difference charge densities around Mn nuclei are allowed in the tetragonal symmetry, which is lower symmetry compared with cubic symmetry. The atomic charges of K and F which are calculated from the MEM charge densities approach electrically neutral state with pressure, whereas the atomic charge of Mn is not changed by pressure. This behavior suggests that the electron charge transfer from F to K increases as the applied pressure increases.

ACKNOWLEDGMENTS

This work has been supported by a Grant-in-Aid for Scientific Research and a Grant-in-Aid for the 21st Century COE from the Ministry of Education, Culture, Science, Sports and Technology of Japan. The SR experiments were performed at SPring-8 BL10XU and BL02B2 with the approval of the Japan SR Research Institute (JASRI).

[1] K. Hirakawa, K. Hirakawa, and T. Hashimoto, J. Phys. Soc. Jpn. **15**, 2063 (1960).
[2] A. Okazaki, Y. Suemune, and T. Fuchikami, J. Phys. Soc. Jpn. **14**, 1823 (1959).
[3] K. Knox, Acta Crystallogr. **14**, 583 (1961).
[4] V. J. Minkiewicz, Y. Fujii, and Y. Yamada, J. Phys. Soc. Jpn. **28**, 443 (1970).
[5] J. Kapusta, P. Daniel, and A. Ratuszna, Phys. Rev. B **59**, 14235 (1999).
[6] A. J. Heeger, O. Beckman, and A. M. Portis, Phys. Rev. **123**, 1652 (1961).
[7] M. Hidaka, N. Ohama, A. Okazaki, H. Sakashita, and S. Yamakawa, Solid State Commun. **16**, 1121 (1975).
[8] A. Gibaud, S. M. Shapiro, J. Nouet, and H. You, Phys. Rev. B **44**, 2437 (1991).
[9] L. J. de Jongh and R. Block, Physica B & C **79**, 568 (1975).
[10] J. M. Ricart, R. Dovesi, C. Roetti, and V. R. Saunders, Phys. Rev. B **52**, 2381 (1995).
[11] R. Dovesi, F. F. Fava, C. Roetti, and V. R. Saunders, Faraday Discuss. **106**, 173 (1997).
[12] E. N. Maslen and N. Spadaccini, Acta Crystallogr., B: **45**, 45 (1989).
[13] A. Sawaoka and C. T. Tomizuka, J. Phys. Soc. Jpn. **36**, 910 (1974).
[14] B. Okai and J. Yoshimoto, J. Phys. Soc. Jpn. **34**, 837 (1973).
[15] K. Gesi and K. Ozawa, J. Phys. Soc. Jpn. **34**, 1698 (1973).
[16] S. Åsbrink, A. Waśkowska, and A. Ratuszna, J. Phys. Chem. Solids **54**, 507 (1993).
[17] S. Åsbrink and A. Waśkowska, Phys. Rev. B **53**, 12 (1996).
[18] Y. Kuroiwa, S. Aoyagi, A. Sawada, J. Harada, E. Nishibori, M. Takata, and M. Sakata, Phys. Rev. Lett. **87**, 217601 (2001).
[19] S. Aoyagi, Y. Kuroiwa, A. Sawada, H. Tanaka, J. Harada, E. Nishibori, M. Takata, and M. Sakata, J. Phys. Soc. Jpn. **71**, 2353 (2002).
[20] Y. Kuroiwa, S. Aoyagi, A. Sawada, E. Nishibori, M. Takata, M. Sakata, H. Tanaka, and J. Harada, J. Korean Phys. Soc. **42**, S1425 (2003).
[21] E. Nishibori, M. Takata, K. Kato, M. Sakata, Y. Kubota, S. Aoyagi, Y. Kuroiwa, M. Yamakata, and N. Ikeda, Nucl. Instrum. Methods Phys. Res. A **467-468**, 1045 (2001).
[22] M. Sakata and M. Sato, Acta Crystallogr., Sect. A: **46**, 263 (1990).
[23] M. Takata, E. Nishibori, and M. Sakata, Z. Kristallogr. **216**, 71 (2001).

[24] E. Nishibori, E. Sunaoshi, A. Yoshida, S. Aoyagi, K. Kato, M. Takata, and M. Sakata, Acta Crystallogr., Sect. A: Found. Crystallogr. **63**, 43 (2007).
[25] M. Sakata, T. Itsubo, E. Nishibori, Y. Moritomo, N. Kojima, Y. Ohishi, and M. Takata, J. Phys. Chem. Solids **65**, 1973 (2004).
[26] K. Kato, Y. Ohishi, M. Takata, E. Nishibori, M. Sakata, and Y. Moritomo, Phys. Rev. B **71**, 012404 (2005).
[27] Y. Amemiya, J. Synchrotron Radiat. **2**, 13 (1995).
[28] P. Norby, J. Appl. Crystallogr. **30**, 21 (1997).
[29] J. Zaleski, G. Wu, and P. Coppens, J. Appl. Crystallogr. **31**, 302 (1998).
[30] *International Tables for Crystallography*, edited by A. J. C. Wilson (Kluwer Academic, Dordrecht, 1995), Vol. C.
[31] H. Toraya, J. Appl. Crystallogr. **23**, 485 (1990).
[32] H. Tanaka, M. Takata, E. Nishibori, K. Kato, T. Iishi, and M. Sakata, J. Appl. Crystallogr. **35**, 282 (2002).